AIAA JOURNAL
Vol. 39, No. 10, October 2001

Numerical Simulations of Sound from Confined Pulsating Axisymmetric Jets

W. Zhao,* S. H. Frankel,† and L. Mongeau‡
Purdue University, West Lafayette, Indiana 47907

Numerical simulations of the near-field flow and far-field sound radiation in confined pulsating axisymmetric low-Mach-number jets were performed. The geometry resembled a round duct with either a converging or diverging rigid orifice separating the upstream and downstream regions. A sinusoidal inlet velocity time history was imposed to generate the pulsating flow. The objectives were to 1) investigate flow patterns and sound sources, 2) assess Lighthill's acoustic analogy for far-field sound predictions in ducts, and 3) examine the effects of orifice shape on the flow and acoustic behavior. The diverging orifice case featured flow separation and reattachment resulting in a complex vortical flow within the orifice, in contrast to the converging orifice case. Both orifices produced unstable pulsating jets with vortex roll up and pairing downstream of the orifices. Agreement between directly computed sound and Lighthill's acoustic analogy was excellent for both orifices. Using the Lighthill acoustic analogy, three sound-generating mechanisms were identified. The first was a monopole source mainly caused by the fluctuating volume velocity. The second was a dipole source caused by the unsteady forces exerted on the duct walls. The third was a quadrupole sound source caused by the presence of vortex pairing. The main difference between the acoustic signal in the diverging and converging orifice cases was related to the frequency content of the quadrupole source caused by vortex pairing, which was higher in the diverging case because of the more intense vortical flow.

I. Introduction

THERE are many important engineering and physiological applications where confined pulsating vortical jet flows are generated. In engineering this type of flowfield is found in pulsed combustors or in steady combustors undergoing combustion-driven oscillations. In either case the volume flow rate at the inlet of the combustor varies with time, and strong acoustic waves are present inside the combustor. Other application areas that involve confined unsteady flows include hydraulic transients in valves or pumps and the transient response of gas turbine engines. Among physiological flows phonation or human speech production involves the interaction between a pulsating air jet and the vocal tract.[1] In phonation the lungs provide a high-pressure air source that establishes self-sustained oscillations of the glottis (or vocal folds) in the vocal tract and a confined pulsating air jet. The glottis is a slit-like orifice between the vocal cords located in the airway and connected to the vocal tract. A typical sequence of the motion of the vocal cords is sketched in Fig. 1. Initially the glottis is almost closed, and high-pressure air from the lung forces it to open. A starting jet forms, and the pressure around the vocal cords decreases according to Bernoulli's equation. The glottis is then forced to close again, and the cycle repeats. There are three main shapes the glottis takes during the open part of the cycle: diverging, uniform, and converging. The acoustic waves generated by this flow, which represent the main source for speech, are effectively filtered by the articulators forming the vocal tract downstream, such as the mouth and nasal cavity, before being radiated from the lips. It is believed that the interaction between the flowfield and the glottal walls has an important impact on voice production.[1]

There have been a number of recent studies employing computational aeroacoustics techniques for free shear layers and jet[2–6] and flow past cavities,[7] but there have not been many studies on confined flows. Recent experimental studies of the aeroacoustics of diffusers have revealed the importance of flow separation on the intensity and spectra of the radiated sound.[8–10]

Several previous studies have motivated the present work. McGowan[11] pursued the use of an aeroacoustic approach to study the source of sound during phonation. He postulated that, in addition to the unsteady volume velocity monopole source, an oscillating force arises from an interaction between vortical structures shed from the glottis and the velocity field itself. This results in a dipole acoustic source. In a pair of recent papers, Barney et al.[12] and Shadle et al.[13] made measurements in a dynamic mechanical model of the larynx and vocal tract. A pair of sinusoidally oscillating shutters modulated an otherwise steady airflow. They found evidence of a vortex train, which generated sound caused by interactions with the tract geometry downstream of the shutters. Finally, Hofmans[14] experimentally, analytically, and numerically studied vortex generated sound in confined ducts. They studied impulsively started flows through a rigid model of the vocal folds, thus capturing the first part of the cycle. The numerical simulations were primarily based on an incompressible vortex method, and they did not attempt to capture the acoustic field numerically.

In this study the geometry and flow conditions for the numerical simulations were chosen to mimic, as closely as possible within the limitations of the numerical methods, the pulsating flow through the human glottis and vocal tract. The main difference between the present simulations and the actual process of phonation is related to the fact that a rigid model of the glottis was used, and therefore sinusoidal flow pulsations upstream of the glottis must be imposed to generate the pulsating flow. This was intended as a first step before considering the effects of moving walls and flow-structure interactions. It is believed that the computational methods utilized and the results obtained will also be useful for other applications relevant to the aircraft industry. For clarity, the pseudoglottis will be referred to as the "orifice" and the pseudo-vocal-tract as the "duct" in the following.

Two geometrically axisymmetric cases were studied. The first involves a diverging orifice shape, and the second involves a converging one. A sufficiently long computational domain was used such that the acoustic signal computed near the outflow boundary was accurate for at least one forcing period. Lighthill's acoustic analogy was used to identify the different sound-generating mechanisms in both cases, and the predictions were compared with the directly computed results.

II. Computational Approach

A. Numerical Method

The compressible Navier–Stokes equations in a curvilinear coordinate system in the x–r (axial-radial) plane were used as the

Received 7 June 2000; revision received 18 April 2001; accepted for publication 30 April 2001.

*Postdoctoral Researcher, School of Mechanical Engineering.
†Associate Professor, School of Mechanical Engineering; frankel@ecn.purdue.edu. Senior Member AIAA.
‡Associate Professor, School of Mechanical Engineering. Member AIAA.

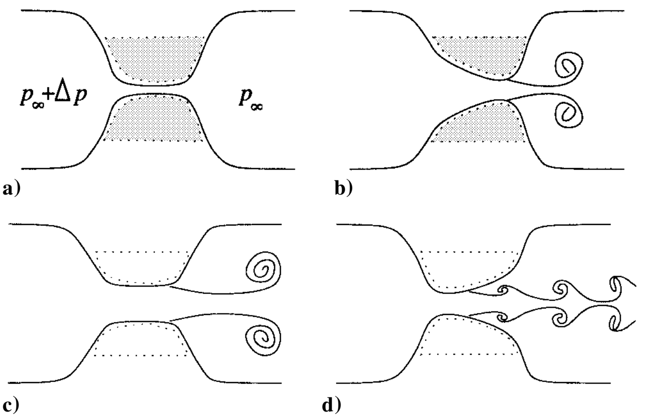

Fig. 1 Idealized sketch illustrating a time sequence of the motion of the human glottis.

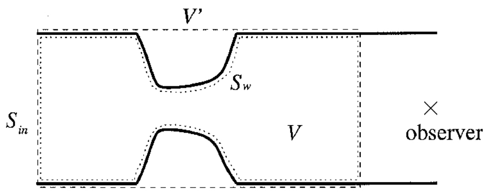

Fig. 2 Sketch of the integral domains and surfaces involving the Lighthill's acoustic analogy.

governing equations. Ideal gas and constant thermodynamic and transport properties were assumed. A sixth-order compact difference scheme[15] was used for spatial discretization, and the fourth-order Runge–Kutta method was used for time marching. No-slip, adiabatic boundary conditions were specified on the duct wall boundary. Nonreflecting, characteristic-based boundary conditions[16] were used at the outflow boundary. A uniform velocity profile with a sinusoidal time variation was specified at the inflow boundary with other variables computed using the nonreflecting boundary condition treatment.

B. Acoustic Analogy

The geometric configuration considered in this application of the acoustic analogy represents an infinite uniform duct. The throat region is considered a solid body within the duct, as depicted in Fig. 2. The wall surface is assumed to be described by

$$S(\boldsymbol{x}, t) = 0 \tag{1}$$

where it is further assumed that $S > 0$ represents the domain inside the duct and $S < 0$ represents the area outside of the duct. The Ffowcs Williams–Hawkings equation accounts for the effect of solid surfaces and takes the form[17]

$$\left(\frac{\partial^2}{\partial t^2} - c_\infty^2 \nabla^2\right)[H(S)\rho'] = \frac{\partial^2}{\partial x_i \partial x_j}[T_{ij} H(S)] - \frac{\partial}{\partial x_i}[F_i \delta(S)] + \frac{\partial}{\partial t}[Q\delta(S)] \tag{2}$$

where $H(S)$ is the Heaviside function, $\delta(S)$ is the Dirac-δ function, and

$$T_{ij} = \rho u_i u_j + \delta_{ij}\left(p' - c_\infty^2 \rho'\right) - \sigma_{ij} \tag{3}$$

is the Lighthill's source tensor. F_i and Q are defined as

$$F_i = [p\delta_{ij} + \sigma_{ij} + \rho u_i(u_j - v_j)]\frac{\partial S}{\partial x_j} \tag{4}$$

$$Q = [\rho_\infty v_i + \rho(u_i - v_i)]\frac{\partial S}{\partial x_i} \tag{5}$$

Here v_i is the wall surface velocity, $\rho' = \rho - \rho_\infty$, and $p' = p - p_\infty$, with ρ_∞, p_∞, and c_∞ representing the density, pressure, and sound speed in the far field, respectively. In the present study only the no-slip wall condition was considered, i.e., $v_i = u_i$ on the surface $S = 0$. Thus,

$$F_i = (p\delta_{ij} + \sigma_{ij})\frac{\partial S}{\partial x_j} \tag{6}$$

$$Q = \rho_\infty v_i \frac{\partial S}{\partial x_i} \tag{7}$$

For $S > 0$ Eq. (2) is in fact the Lighthill's equation[18] with additional sources because of the presence of rigid boundaries. Equation (2) is exact in the sense that it is only a reformulation of the governing equations. The main assumptions in the application of the acoustic analogy are that the sources of sound are all contained within a certain region and that there is no interaction between the radiated sound and the flow. Based on these assumptions, Eq. (2) has a solution in terms of Green's function:

$$p' = \int_{-\infty}^{t} \iiint_{V'} G(\boldsymbol{x}, t; \boldsymbol{y}, \tau)\left\{\frac{\partial^2}{\partial x_i \partial x_j}[T_{ij} H(S)] - \frac{\partial}{\partial x_i}[F_i \delta(S)] + \frac{\partial}{\partial t}[Q\delta(S)]\right\} \mathrm{d}V'(\boldsymbol{y})\,\mathrm{d}\tau \tag{8}$$

where V' is the volume including both the source region V and the solid bodies inside the duct and where the one-dimensional, low-frequency Green's function in a uniform duct was introduced:

$$G(\boldsymbol{x}, t; \boldsymbol{y}, \tau) = (c_\infty/2A_0)H[t - \tau - (x_1 - y_1)/c_\infty] \tag{9}$$

where A_0 is the cross-sectional area of the duct. Viscous dissipation of the acoustic waves and convection effects as the waves propagate in the duct are neglected in the Green's function, which introduces potential errors in predictions from the acoustic analogy. Therefore, the application of the acoustic analogy is limited to the cases where the acoustic wavelength is much larger than the size of the dominant source region, and the axial velocity of the mean flow in the downstream of the duct is much smaller than the sound speed. After some manipulations the main result of this section can be written as[14,17]

$$\begin{aligned} p' = {} & \frac{1}{2c_\infty A_0}\frac{\partial}{\partial t}\iiint_V [T_{11}]_{t^*}\,\mathrm{d}V(\boldsymbol{y}) \quad \text{(I)} \\ & - \frac{1}{2A_0}\iint_{S_w}[p\delta_{1j} - \sigma_{1j}]_{t^*} n_j\,\mathrm{d}S(\boldsymbol{y}) \quad \text{(II)} \\ & - \frac{1}{2A_0}\iint_{S_w}[\rho_\infty c_\infty v_j]_{t^*} n_j\,\mathrm{d}S(\boldsymbol{y}) \quad \text{(III)} \\ & + \frac{1}{2A_0}\iint_{S_{in}}[p' + \rho_\infty c_\infty u_1]_{t^*}\,\mathrm{d}S(\boldsymbol{y}) \quad \text{(IV)} \end{aligned} \tag{10}$$

where $t^* = t - \tau - (x_1 - y_1/c_\infty)$ is the retarded time, V is the volume of source region, S_w is the surface area of the duct wall, S_{in} is the inlet surface, and n_j is the unit vector normal to the surface. The physical meaning of the four terms is as follows: term (I) is the quadrupole source caused by unsteady flow inside the duct; term (II) is the dipole source caused by the unsteady forces exerted on the walls; term (III) is the monopole source caused by the motion of the wall in the throat region, if the wall is fixed this term is zero; and term (IV) is the monopole source enforced at the inlet.

C. Simulation Details

The shape of the circular duct was defined by the function

$$r_w(x) = \frac{D_0 - D_g}{4}\tanh\left(\frac{b|x|}{D_g} - \frac{bD_g}{|x|}\right) + \frac{D_0 + D_g}{4} + \frac{1}{2}\tan(\alpha)(x + cD_g)\left[1 + \tanh\left(\frac{b|x|}{D_g} - \frac{bD_g}{|x|}\right)\right] \tag{11}$$

where D_g is the minimum orifice diameter; $D_0 = 2.5D_g$ is the diameter of the uniform duct; $b = 1.4$ and $c = \pm 0.39$ for diverging and converging cases, respectively, are constants; and $\alpha = \pm 20$ deg is the open angle of the orifice. The computational domain extends from $x = -4D_g$ to $85D_g$, and $x = 0$ is at the center of the orifice. The curvilinear coordinate system utilized takes the form

$$\xi = x \tag{12}$$

$$\zeta = r/r_w(x) \tag{13}$$

The time-varying velocity profile specified at the inlet was given by

$$u_{\text{in}}(r, t) = U_0(t)\tanh[40/D_g(D_0 - r)] \tag{14}$$

This is an almost uniform profile with a time-varying maximum value $U_0(t)$, which is given by

$$U_0(t) = 0.02004U_M - 0.02U_M\cos(2\pi f_0 t) \tag{15}$$

where f_0 is the forcing frequency and U_M is the estimated maximum velocity at the throat. A set of values for f_0, U_M, and D_g, typical for speech production, were chosen as 125 Hz, 40 m/s, and 0.004 m, respectively.[1] The corresponding Strouhal number is $Sr = f_0 D_g/U_M = 0.0125$. The Mach number M corresponding to U_M was artificially increased from about 0.117 to 0.2 to improve the computational efficiency of the simulations. For such low subsonic-Mach-number flows little effect on the flowfield is expected as a result of this change in Mach number. The Reynolds number based on the mean velocity and the radius at the throat was 3×10^3. Generally, this Reynolds numbers implies a turbulent jet, which requires a fully three-dimensional simulation to capture vortex stretching and all of the sound sources. However, a three-dimensional direct numerical simulation or even a large eddy simulation for this type of pulsating jet in a complex geometry is prohibitively expensive with current computer resources. The current simulation allows us to accurately predict all of the sound sources other than turbulence. It is believed that an axisymmetric simulation will help understanding the aerodynamics and aeroacoustics in human speech production. In addition to representing a model for the human vocal tract, the geometry and flow conditions studied here are also relevant to the general case of unsteady (pulsatile), low-speed flow in a duct through a nozzle or a diffuser.

A uniform grid was used in the ζ direction, and a nonuniform grid was used in the ξ direction. Grid clustering was used in the orifice region to resolve the complex flow structures expected there. A coarser grid was used near the outflow boundary because the vortices become considerably weaker as they propagate downstream. The maximum ratio of adjacent grid spacings in this study was less than 5% in order to minimize dispersion errors associated with grid stretching. The base grid used for all of the cases presented in this study was 720×120. A sample computational grid (all grid points not shown for clarity) is shown in Fig. 3.

To address one aspect of numerical accuracy for the current simulations, a grid-convergence study was conducted for the diverging orifice case. The computational domain was shortened ($-4D_g \leq x \leq 2.5D_g$) to decrease the computational cost. Uniform grids were employed in both directions to assess possible dispersion errors associated with grid stretching mentioned earlier. Simulations on a finer grid with 320×160 points and a coarser grid with 240×80 points were marched to $t = 26.67D_g/U_M$ (55,000 time steps for the fine grid case), when the leading vortex ring was about to leave the shortened computational domain. Radial profiles of the

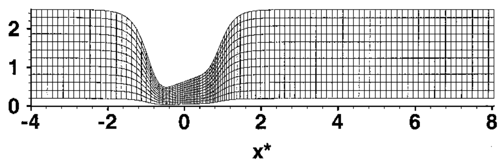

Fig. 3 Model geometry and computational grid for the diverging orifice case. (Only part of the computational domain is shown.)

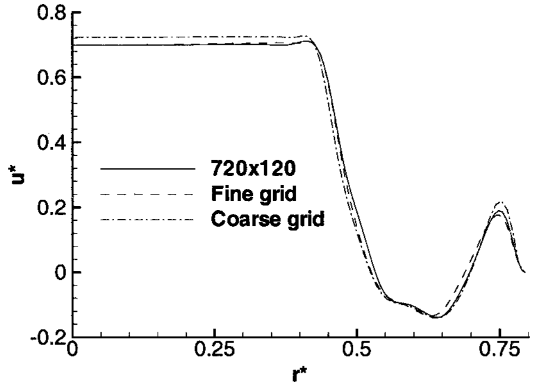

$x = 0.40D_g$

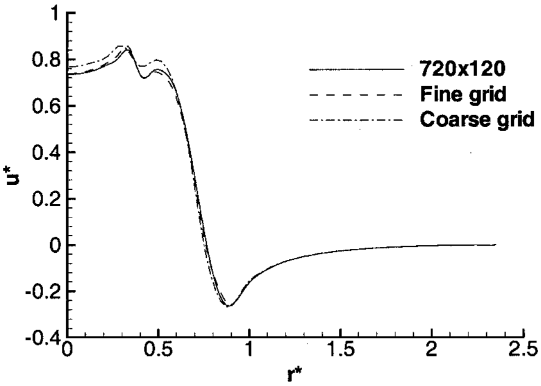

$x = 1.43D_g$

Fig. 4 Comparison of radial profiles of axial velocity at $t^* = 26.67$ for three different grids.

axial velocity at $x = 0.40D_g$ and $1.43D_g$ are shown in Fig. 4 for the three different grid cases. The first axial location is just inside the orifice, where the flowfield features separation and reattachment (to be discussed in more detail in the next section), whereas the second location passes through the center of the leading vortex ring. The agreement between predictions obtained on the 720×120 grid and the finest grid is excellent at both axial locations. Even the coarsest grid yields reasonable predictions. The base grid appears to be adequate for the current simulations.

In terms of validation, the computer code used in the present study has also been used to predict impulsively started jets[19] and freejet sound radiation.[5] Predictions from these two studies have been in very good agreement with previous experimental data and numerical studies.

III. Results

All of the parameters and results presented in this study are in nondimensional form unless otherwise mentioned. The characteristic scales used to nondimensionalize the variables were the diameter of the orifice D_g, the estimated peak velocity U_M, and the initial quiescent values of the density and temperature. The nondimensionalized forcing period was $T_0^* = 80$.

A. Near-Field Flow Analysis

A time sequence displaying instantaneous vorticity contour plots for the diverging orifice case is shown in Fig. 5. At $t^* = \frac{1}{6}T_0^*$ a thin shear layer is formed around the orifice, and the flow is about to separate at the diverging point. At time $t^* = \frac{2}{6}T_0^*$ a starting jet with a leading vortex ring is generated, and a second vortex is observed to form near the end of the orifice wall. At $t^* = \frac{3}{6}T_0^*$, $\frac{4}{6}T_0^*$, and $\frac{5}{6}T_0^*$ the volume flux through the orifice is near its peak value. The flowfield features the Kelvin–Helmholtz roll up of very strong vortices and the pairing of the vortices along the jet. After that the volume flux decreases, and only very weak discrete vortices are observed near the orifice. The vortical structures at $t^* = \frac{7}{6}T_0^*$ are very similar to

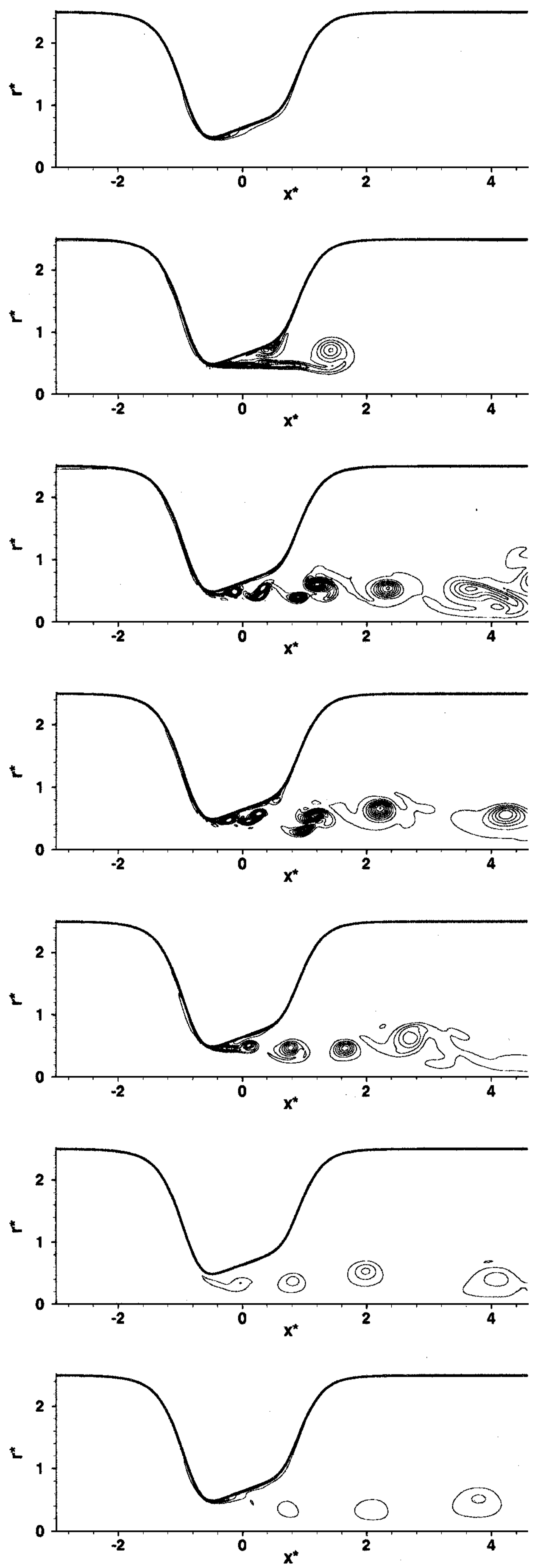

Fig. 5 Time sequence of instantaneous vorticity contour plots for the diverging orifice case. From top to bottom, $t^* = \frac{1}{6}T_0^*, \frac{1}{6}T_0^*, \ldots, \frac{7}{6}T_0^*$. Contour levels: Min = 5, Max = 20; number of levels is 15.

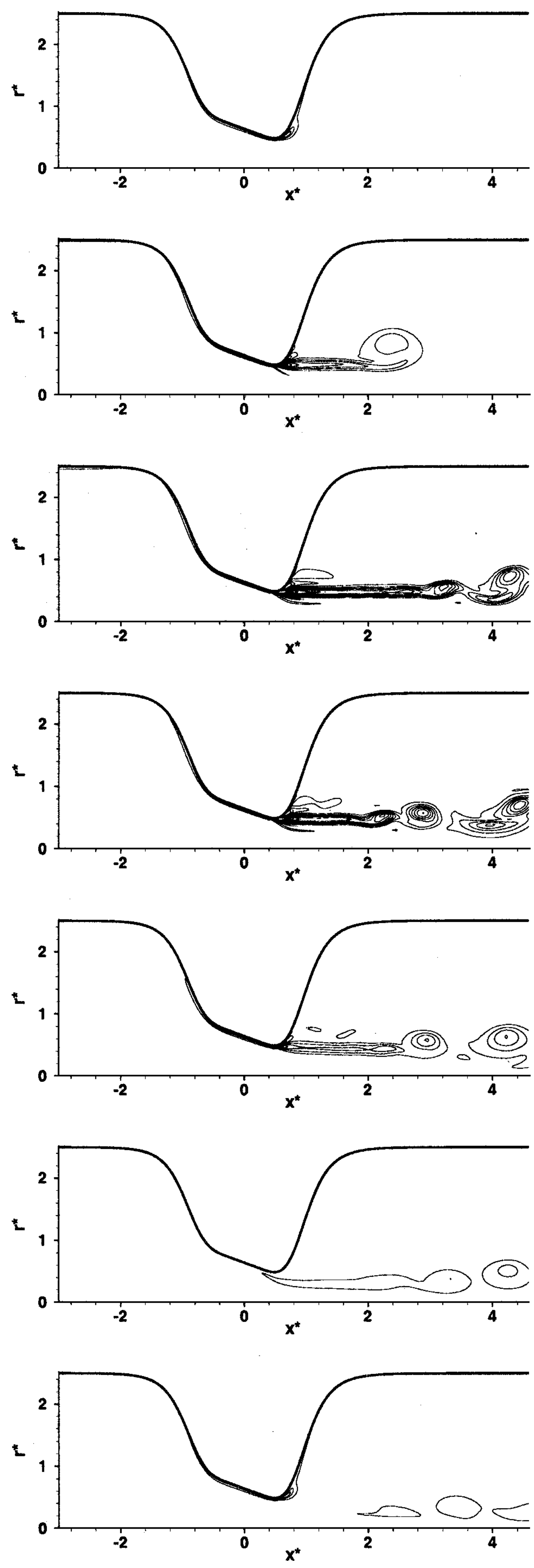

Fig. 6 Time sequence of the instantaneous vorticity contour plots for the converging orifice case. From top to bottom, $t^* = \frac{1}{6}T_0^*, \frac{1}{6}T_0^*, \ldots, \frac{7}{6}T_0^*$. Contour levels: Min = 5, Max = 20, number of levels is 15.

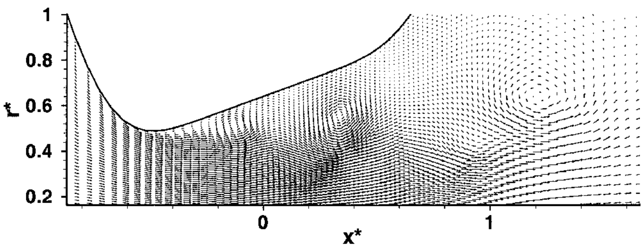

Fig. 7 Close-up of velocity vectors near the orifice at $t = 0.5T_0^*$ for the diverging orifice case.

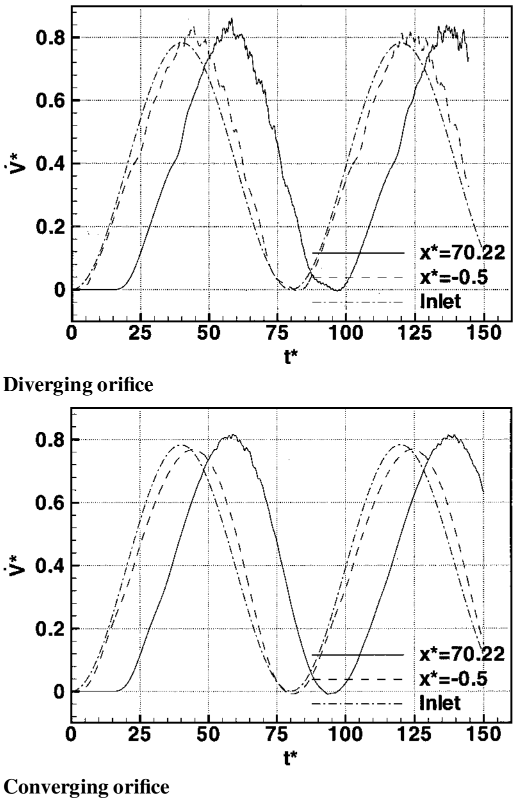

Fig. 8 Volume flow rates at the inlet, throat ($x^* = -0.5$), and near the outflow boundary ($x^* = 70.22$) for the two cases.

those at $t^* = \frac{1}{6}T_0^*$ except for the vortex wake downstream of the orifice.

A similar sequence of vorticity contour plots is shown for the converging orifice case in Fig. 6. In this case the flow separates downstream of the orifice as a result of the converging shape and favorable pressure gradient within the orifice. At $t^* = \frac{2}{6}T_0^*$ a vortex ring is also generated, but the trailing jet is more stable than in the diverging orifice case. Secondary vortices emerge downstream of the orifice. Vortex pairing is also observed within the jet.

For the diverging orifice case the flow separates at the inlet of the orifice. Small, but intense, vortices are formed as a result of the small opening of the orifice. The interaction between the vortices and the jet generates a complex flowfield inside the orifice. A enlarged view of the velocity vectors within the orifice is shown in Fig. 7. The concentrated vortices are convected downstream with the jet, affecting the jet stability.

The volume flow rate at axial positions, $x^* = -4, -0.5$, and 70.22, is shown in Fig. 8 for both the diverging and converging cases. The first axial location corresponds to the inlet boundary, the second to the throat (minimum area) in the diverging case, and the third is far downstream of the orifice near the outflow boundary. The volume flow rate enforced at the inlet is a sinusoidal function of time for both cases. For the diverging orifice case the flow separation and reattachment process produces vortices that change the effective area of the orifice just downstream of the throat. This also changes the drag force exerted by the flow. These changes are responsible for small oscillations in volume flux at the throat that are not present at the inlet. For the converging orifice case these oscillations are smaller because the flow does not separate until the end of orifice, and the measurement location is at the throat region of the diverging case. Far downstream of the orifice, the volume flow rate can be considered the acoustic signal in the duct. In both cases the volume flow rate near the outflow boundary is slightly higher than the value inside the orifice, which suggests additional acoustic sources may be present in the duct downstream of the orifice. This is discussed in the next subsection.

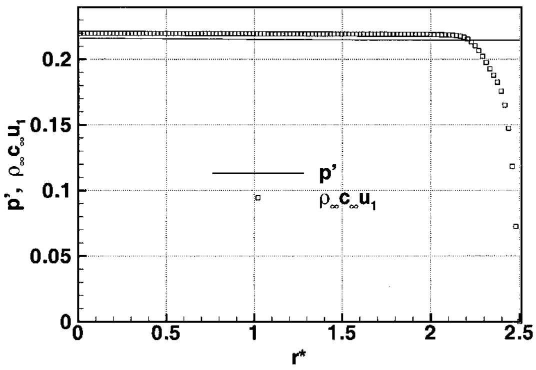

Fig. 9 Radial profiles of the acoustic pressure and axial velocity at $x^* = 70.22$ for the diverging orifice case.

B. Far-Field Sound Radiation

To record the far-field acoustic signal, a numerical microphone was placed at $x^* = 70.22$ near the duct wall. Figure 9 shows instantaneous radial profiles of the acoustic variables p' and $\rho_\infty c_\infty u_1$ at $x^* = 70.22$ at $t^* = 133.4$. The profile of the acoustic pressure is practically uniform, suggesting planar waves. In the axial velocity profile a boundary layer can be observed near the wall as a result of the specified no-slip boundary condition. Outside the boundary layer the velocity is also uniform. Approximately a 2% difference is observed between the values of p' and $\rho_\infty c_\infty u'$ in the uniform region near the centerline. Previous numerical simulations of sound radiation from shear layers have shown that mean flow values, such as pressure, drifted with time when the nonreflecting outflow boundary conditions were employed.[2,3] Thus, the aforementioned differences were attributed to small changes in the mean density and sound speed.

A comparison between the directly computed acoustic pressure p' and the Lighthill acoustic analogy prediction is plotted in Fig. 10a for the diverging orifice case. The acoustic signal deviated from the sinusoidal function imposed for the volume flux at the inlet. High-frequency components of sound pressure are visible near the peak value. The results from the two methods almost collapse on each other. To better appreciate the agreement between the two predictions, a close-up of the first peak in the plot is shown in Fig. 10b. The agreement is excellent. The acoustic analogy slightly underpredicts the directly computed result. This is attributed to the already mentioned thin boundary layer, which forms along the walls of the uniform sections of the duct. This reduces the effective area of the duct. Hence, the value of A_0 used in Eq. (10) results in a sound-pressure underprediction using the acoustic analogy. A small phase shift can also be detected in the acoustic analogy predictions. This is attributed to the small variation in sound speed, mentioned earlier, and mean flow convection effects on the acoustic wave.

Figure 11 shows the acoustic pressure at the same location for the converging orifice case. The result is very similar to that for the diverging orifice case, except the high-frequency components near the peak value are smaller than those for the diverging case. This will be explained shortly.

The Lighthill acoustic analogy was then used to predict the contribution to sound radiation from the different source terms in Eq. (10). The results are shown in Fig. 12. For both the diverging and converging cases the monopole source at the inlet [term (IV)] and the dipole source caused by the unsteady forces exerted on the wall [term (II)] are the dominant sources. These two sources are perfectly out

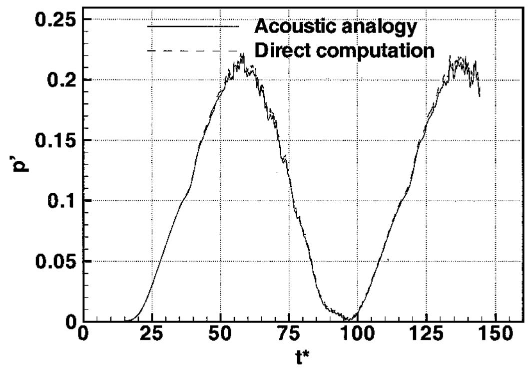

a) Full scale

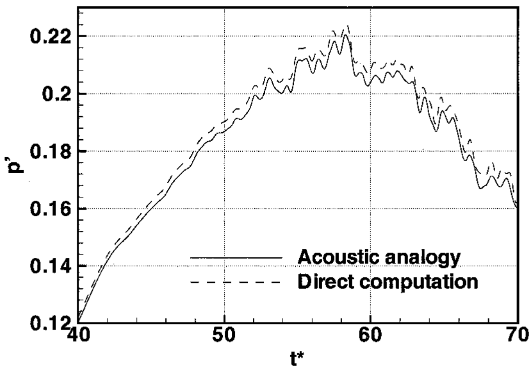

b) Close-up

Fig. 10 Comparison of acoustic signal between the directly computed results and predictions from Lighthill's acoustic analogy at axial position $x^* = 70.22$ for the diverging orifice case.

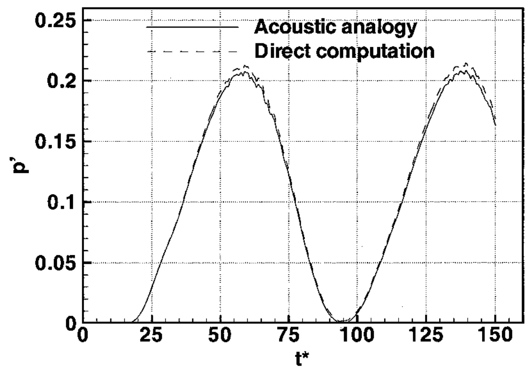

Fig. 11 Comparison of acoustic signal between the directly computed results and predictions from Lighthill's acoustic analogy for the converging orifice case.

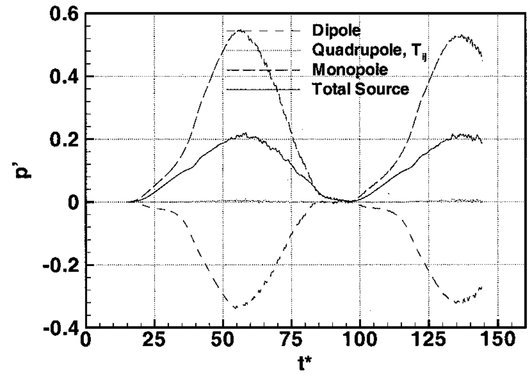

Diverging orifice

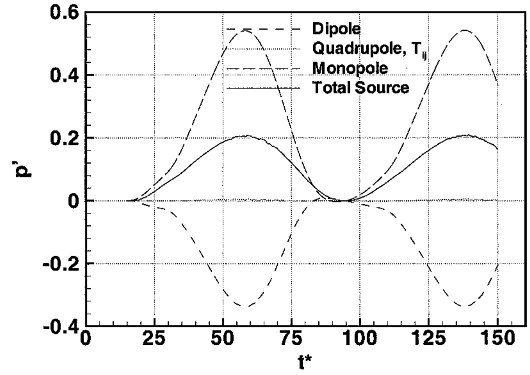

Converging orifice

Fig. 12 Contribution to sound radiation from different sources.

of phase. The monopole source here is not equal to the volume flux contribution at the inlet. At the beginning of the simulation, the volume flux imposed at the inlet generates an incident acoustic wave that propagates downstream. When it reaches the orifice, an acoustic wave is reflected and propagates back toward the inflow boundary. The inflow boundary conditions are reflecting boundary conditions because the volume flux is enforced. The reflecting wave from the orifice reflects again at the inlet. The overall acoustic pressure wave entering the computational domain is $\frac{1}{2}(p'_{\text{in}} + \rho_\infty c_\infty u_{\text{in}})$. This is consistent with term (IV) in Eq. (10). The magnitudes of the contribution from the quadrupole source [term (I)] are about one order lower than those of the monopole and dipole sources. High-frequency oscillations are observed in the monopole and dipole sources contribution for the diverging orifice case, whereas the contribution from these sources for the converging orifice case is very smooth. It has already been shown in Fig. 5 that there exists a very strong interaction between the vortical structure and the orifice wall after flow separation. This interaction causes pressure oscillations on the wall, which contribute to the dipole source. For the converging orifice case, however, vortices are formed several D_g downstream of the orifice. The vortices are far away from the wall. Thus no high-frequency oscillations are observed in the monopole and dipole sources.

Mitchell et al.[3] showed that the dominant sound source in an axisymmetric steady free jet was vortex pairing, where only quadrupole source exists. Neglecting the entropy source and the viscous stress in the Lighthill's source tensor and using the compact source assumption (only considering low-frequency sound), term (I) in Eq. (10) can be rewritten as

$$(\text{I}) = \frac{1}{2c_\infty A_0}\frac{\partial}{\partial t}\left[\iiint_V \rho u_1^2\,\mathrm{d}V(\boldsymbol{y})\right]_{t^*} \tag{16}$$

It is associated with the first-order time derivative of the total axial kinetic energy of the fluid inside the control volume. Thus, for the pulsating jets considered in this study the total axial kinetic energy change in the duct, because of its pulsating nature, acts like a low-frequency quadrupole source, in additional to the high-frequency source caused by vortex pairing in the jet. The sound-pressure contribution from the quadrupole source is shown in Fig. 13. During the early stage of one cycle, the quadrupole source contribution increases as the volume flux through the orifice increases. When the volume flux reaches a certain value, secondary vortices are formed inside the jet and subsequently pair with each other, which accounts for the high-frequency sound radiation from the quadrupole source. The frequency of vortex pairing sound radiation for the diverging orifice case is higher than for the converging orifice case. This is consistent with the vortical structure shown in Figs. 5 and 6. The jet formed in the diverging orifice case is more unstable, and vortex pairing occurs inside the orifice when the shear layer is still very thin, and consequently has a higher frequency.

The magnitude of the sound radiation from the quadrupole source is only about $\frac{1}{25}$ times the total acoustic pressure. However, recent large eddy simulation of a subsonic round jet by Zhao et al.[20] showed that the sound radiated from a turbulent jet is about one order higher than that radiated from an axisymmetric jet under the same flow conditions. Therefore, the sound radiation from the quadrupole sources may be much higher if the jet transitions to turbulence and thus can

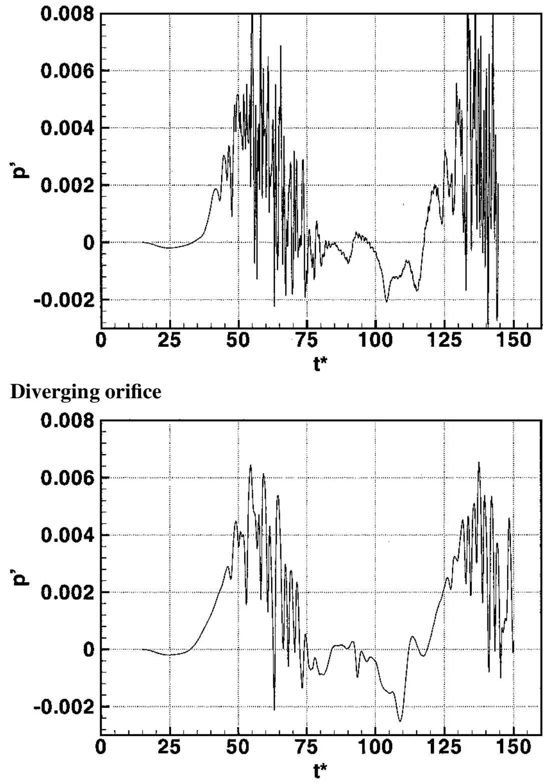

Converging orifice

Fig. 13 Sound radiation from the Lighthill source tensor T_{ij}.

contribute significantly to speech production or other engineering applications with similar flow conditions.

IV. Conclusions

The sound radiated from pulsating jets inside a simplified vocal tract model was simulated by numerically solving the Navier–Stokes equations. Two cases were studied: one with a diverging orifice shape and one with a converging shape. For the diverging orifice case the flow separates at the inlet of the orifice. It shows a very complex vortical structure inside the orifice caused by the interaction between the orifice wall boundary and the impulsively started jet. For the converging orifice case the starting jet is more stable, and Kelvin–Helmholtz-type vortices are formed several D_g downstream the orifice. Lighthill's acoustic analogy was then applied to identify the sound sources. The predictions from the acoustic analogy were in excellent agreement with the directly computed results. The dominant sound sources were the monopole source at the inlet and the dipole source caused by unsteady forces exerted on the wall boundary. The shape of the orifice does not have a significant effect on these two sources, although high-frequency oscillations are observed in monopole and dipole radiation for the diverging orifice case as a result of the interaction between the vortices and the orifice wall. The quadrupole source contributes mainly to the high-frequency sound radiation. The frequency of the quadrupole source radiation of the diverging orifice case was higher than that of the converging orifice case.

Acknowledgments

This work is supported by Research Grant 5 RO1 DC03577-02 from the National Institute of Deafness and Other Communication Disorders, National Institutes of Health. Supercomputer time on the SGI Origin 2000 is provided by the National Center for Supercomputer Applications under Grant CTS980030N and the Computer Science Department at Purdue University.

References

[1]Flanagan, J. L., *Speech Analysis, Synthesis, and Perception*, Springer-Verlag, New York, 1972.

[2]Colonius, T., Lele, S. K., and Moin, P., "Sound Generation in a Mixing Layer," *Journal of Fluid Mechanics*, Vol. 330, 1997, pp. 375–409.

[3]Mitchell, B. E., Lele, S. K., and Moin, P., "Direct Computation of the Sound Generated by Vortex Pairing in an Axisymmetric Jet," *Journal of Fluid Mechanics*, Vol. 383, 1999, pp. 113–142.

[4]Freund, J. B., "Noise Sources in a Low-Reynolds-Number Turbulent Jet at Mach 0.9," *Journal of Fluid Mechanics* (to be published).

[5]Zhao, W., Frankel, S. H., and Mongeau, L., "Effect of Spatial Filtering on Sound Radiation from a Subsonic Axisymmetric Jet," *AIAA Journal*, Vol. 38, No. 11, 2000, pp. 2032–2039.

[6]Zhao, W., Frankel, S. H., and Mongeau, L., "Large Eddy Simulations of Sound Radiation from Subsonic Turbulent Jets," *AIAA Journal*, Vol. 39, No. 8, 2001, pp. 1469–1477.

[7]Colonius, T., Basu, A. J., and Rowley, C. W., "Numerical Investigation of the Flow Past a Cavity," AIAA Paper 99-1912, 1999.

[8]Kwong, A. H. M., and Dowling, A. P., "Unsteady Flow in Diffusers," *Journal of Fluids Engineering*, Vol. 116, 1994, pp. 842–847.

[9]Fehse, K. R., and Neise, W., "Low Frequency Sound Generated by Flow Separation in a Conical Diffuser," *European Journal of Mechanics B—Fluids*, Vol. 19, 2000, pp. 637–652.

[10]van Lier, L., Dequand, S., Hirschberg, A., and Gorter, J., "Aeroacoustics of Diffusers: An Experimental Study of Typical Industrial Diffusers at Reynolds Numbers of O(10^5)," *Journal of the Acoustical Society of America*, Vol. 109, No. 1, 2001, pp. 108–115.

[11]McGowan, R. S., "An Aeroacoustic Approach to Phonation," *Journal of the Acoustical Society of America*, Vol. 83, No. 2, 1988, pp. 696–704.

[12]Barney, A., Shadle, C. H., and Davies, P. O. A. L., "Fluid Flow in a Dynamic Mechanical Model of the Vocal" Folds and Tract. I. Measurements and Theory," *Journal of the Acoustical Society of America*, Vol. 105, No. 1, 1988, pp. 444–455.

[13]Shadle, C. H., Barney, A., and Davies, P. O. A. L., "Fluid Flow in a Dynamic Mechanical Model of the Vocal Folds and Tract. II. Implications for Speech Production Studies," *Journal of the Acoustical Society of America*, Vol. 105, No. 1, 1988, pp. 456–466.

[14]Hofmans, G. C. J., "Vortex Sound in Confined Flows," Ph.D. Dissertation, Technical Univ., Eindhoven, The Netherlands, 1998.

[15]Lele, S. K., "Compact Finite-Difference Schemes with Spectral-Like Resolution," *Journal of Computational Physics*, Vol. 103, 1992, pp. 16–42.

[16]Poinsot, T., and Lele, S., "Boundary Conditions for Direct Simulations of Compressible Viscous Flows," *Journal of Computational Physics*, Vol. 101, 1992, p. 104.

[17]Ffowcs Williams, J. E., and Hawkings, D. L., "Sound Generation by Turbulence and Surfaces in Arbitrary Motion," *Philosophical Transactions of the Royal Society of London, Series A*, Vol. A264, 1969, pp. 321–342.

[18]Lighthill, M. J., "On Sound Generated Aerodynamically; I. General Theory," *Proceedings of the Royal Society of London*, Vol. A211, 1952, pp. 564–587.

[19]Zhao, W., Frankel, S. H., and Mongeau, L., "Effects of Trailing Jet Instability on Vortex Ring Formation," *Physics of Fluids*, Vol. 12, No. 3, 2000, pp. 589–596.

[20]Zhao, W., Frankel, S. H., and Mongeau, L., "Large Eddy Simulation of Sound Radiation from a Subsonic Turbulent Jet," AIAA Paper 00-2078, 2000.

K. Kailasanath
Associate Editor